



OPEN PRKD2 as a novel target for targeting the diabetes–osteoporosis nexus

Rongjin Chen^{1,2,3,4,5}, Chenhui Yang^{1,2,3,4,5}, Hefang Xiao^{1,2,3,5}, Ao Yang^{1,2,3}, Changshun Chen^{1,2,3}, Fei Yang^{1,2,3}, Bo Peng^{1,2,3}, Bin Geng^{1,2,3} & Yayi Xia^{1,2,3}✉

Diabetes mellitus (DM) and osteoporosis (OP) co-morbidity (DMOP) pose major health challenges owing to their complex pathophysiological interactions. The aim of this study was to identify and validate key genes implicated in the pathogenesis of both conditions. By employing the Mfuzz time-series gene clustering method combined with transcriptome sequencing of patient serum, we systematically delineated gene expression patterns during the transition from a healthy state through DM to DMOP. These findings were further validated using external datasets, and a series of functional enrichment analyses, gene set enrichment analyses, and immune cell infiltration studies were conducted. Our analyses revealed a distinct progression pattern from a normal state through DM to DMOP, characterized by dynamic gene expression changes. Notably, *PRKD2* emerged as a significantly downregulated gene in DMOP, highlighting its crucial role in disease pathogenesis. Further analyses revealed the involvement of *PRKD2* in key signaling pathways, especially the Wnt and IL-18 pathways, which are critical for bone and glucose metabolism. Validation in cellular and animal models confirmed the role of *PRKD2* in apoptosis and bone metabolism, emphasizing its therapeutic potential. In conclusion, our findings establish *PRKD2* as a pivotal molecule in DMOP, offering fresh insights into its mechanisms and affirming its value as a therapeutic target.

Keywords Diabetes mellitus, Osteoporosis, Gene expression, Therapeutic discovery, Molecular pathway

Type 2 DM comprises a group of metabolic disorders characterized by chronic hyperglycemia and exerts a substantial burden on global health^{1–3}. The prevalence of DM is rising, further exacerbated by global aging trends and lifestyle changes, which also contribute to a lower age of onset^{4,5}. Osteoporosis (OP), known for its adverse effects on bone density and microstructure, leads to bone fragility and a high risk of fractures^{6–8}. The coexistence of DM and OP (DMOP) in patients correlates with higher rates of incidence and complications, posing substantial challenges to healthcare systems worldwide.

The interaction between DM and OP is becoming increasingly apparent, as DM can induce systemic vascular damage and disrupt bone metabolism^{9,10}, thereby increasing the risk of fractures and deteriorating bone quality through the formation of advanced glycation end products and misalignment of collagen fibers¹¹. Such findings have highlighted the complex relationship between metabolic and bone health and encouraged basic and clinical research efforts to uncover the underlying mechanisms.

With the advancement of bioinformatics and computing technology, the development of comprehensive disease databases has become crucial for dissecting the molecular complexity of multifaceted diseases such as DM and OP. These conditions are systemic, involving multiple organs and systems along with a myriad of genes and regulatory pathways, making their interconnections particularly intricate. Thus, synthesizing and reviewing diverse genetic datasets are essential for elucidating the molecular dynamics underlying DM and OP and laying the groundwork for concurrent therapeutic strategies.

The Mfuzz time-series gene clustering method emerges as a key tool for capturing the subtle, gradual changes in gene expression that characterize disease progression^{12,13}. This approach offers a refined perspective on the molecular landscape of DM and OP^{14,15}. In this study, we employed Mfuzz analysis in conjunction with transcriptome sequencing of patient serum to systematically identify gene expression clusters indicative of both increased and decreased risk of DM and its coexistence with OP. This approach allowed us to delineate

¹Department of Orthopedics, The Second Hospital of Lanzhou University, Lanzhou 730030, China. ²Orthopedic Clinical Medical Research Center and Intelligent Orthopedic Industry Technology Center of Gansu Province, Lanzhou 730030, China. ³The Second Clinical Medical School, Lanzhou University, Lanzhou 730030, China. ⁴Department of Orthopedics, Tianshui Hand and Foot Surgery Hospital, Tianshui 741000, China. ⁵Rongjin Chen, Chenhui Yang and Hefang Xiao contributed equally to this work. ✉email: xiayy@lzu.edu.cn

a “Normal–DM–DMOP” progression rule, facilitating the extraction of cluster genes for in-depth analysis. To bolster the validity of our findings, we further verified hub genes using the datasets GSE56815 (OP) and GSE156061 (DM). This comprehensive methodology enriches our research framework and ensures a robust examination of the molecular dynamics underlying DM and OP. By integrating Mfuzz analysis with advanced transcriptome sequencing and data validation techniques, our study provides a detailed molecular landscape of these conditions.

The aim of this study was to identify and validate critical genes involved in the pathogenesis of DM and OP, enhancing our molecular understanding and supporting personalized and precision medical approaches. Our findings reveal novel diagnostic markers and therapeutic targets that are expected to facilitate individual disease risk prediction and guide innovative treatment strategies to manage disease progression. Furthermore, by employing Mfuzz time-series gene clustering, we report the effectiveness of advanced methodologies for gene expression analysis and contribute to the field of bioinformatics. (Fig. 1).

Results

Screening DEGs in public datasets

Principal component analysis of GSE156061 and GSE56815 showed good discrimination from the control group (Fig. 2a,b). After matrix standardization and differential analysis (Fig. 2c,d), 242 common DEGs were upregulated in GSE156061 and GSE56815 and 288 DEGs were downregulated (Fig. 2e,f). The bottleneck method

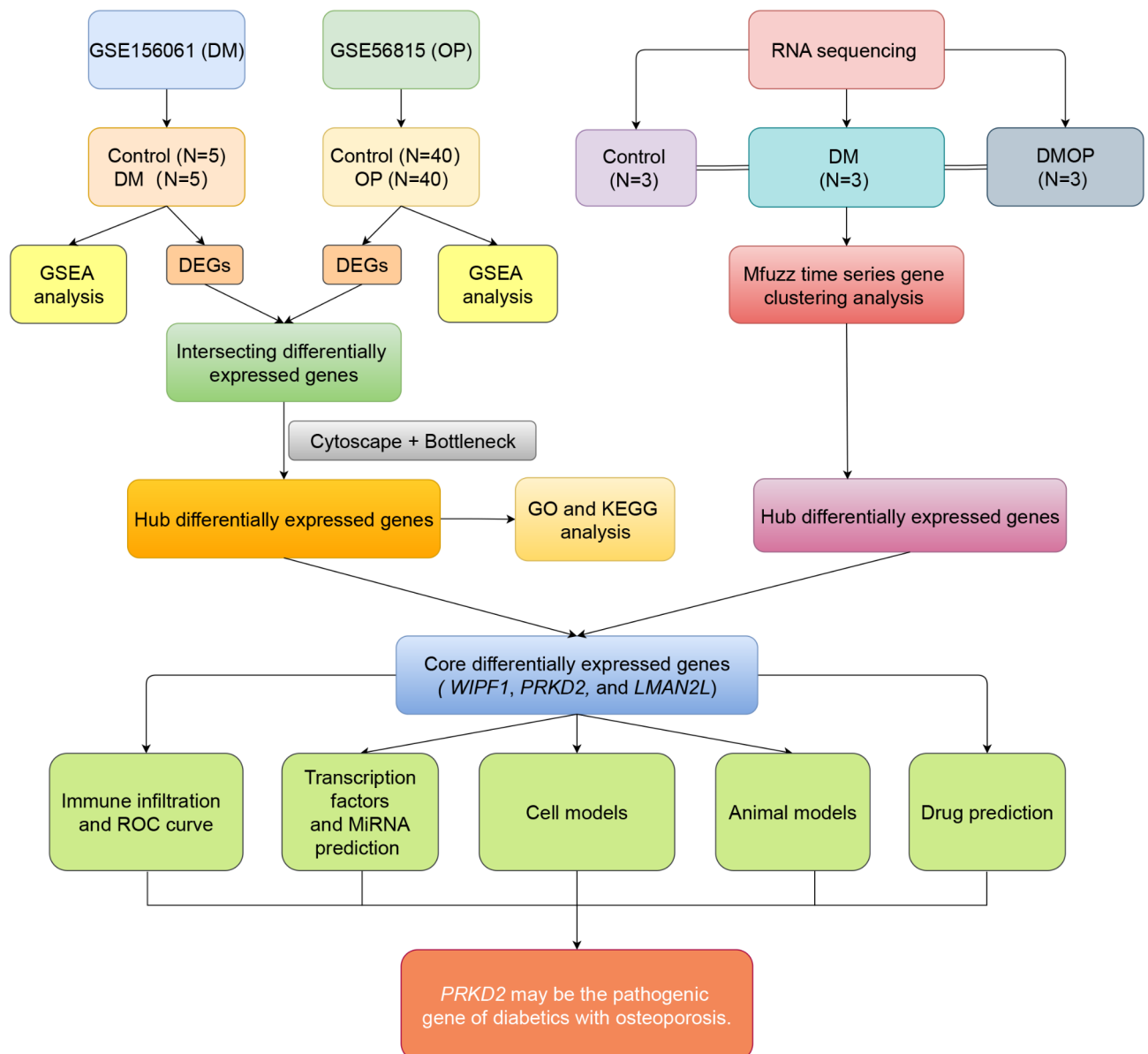


Fig. 1. Flowchart of the methodology employed in this study.

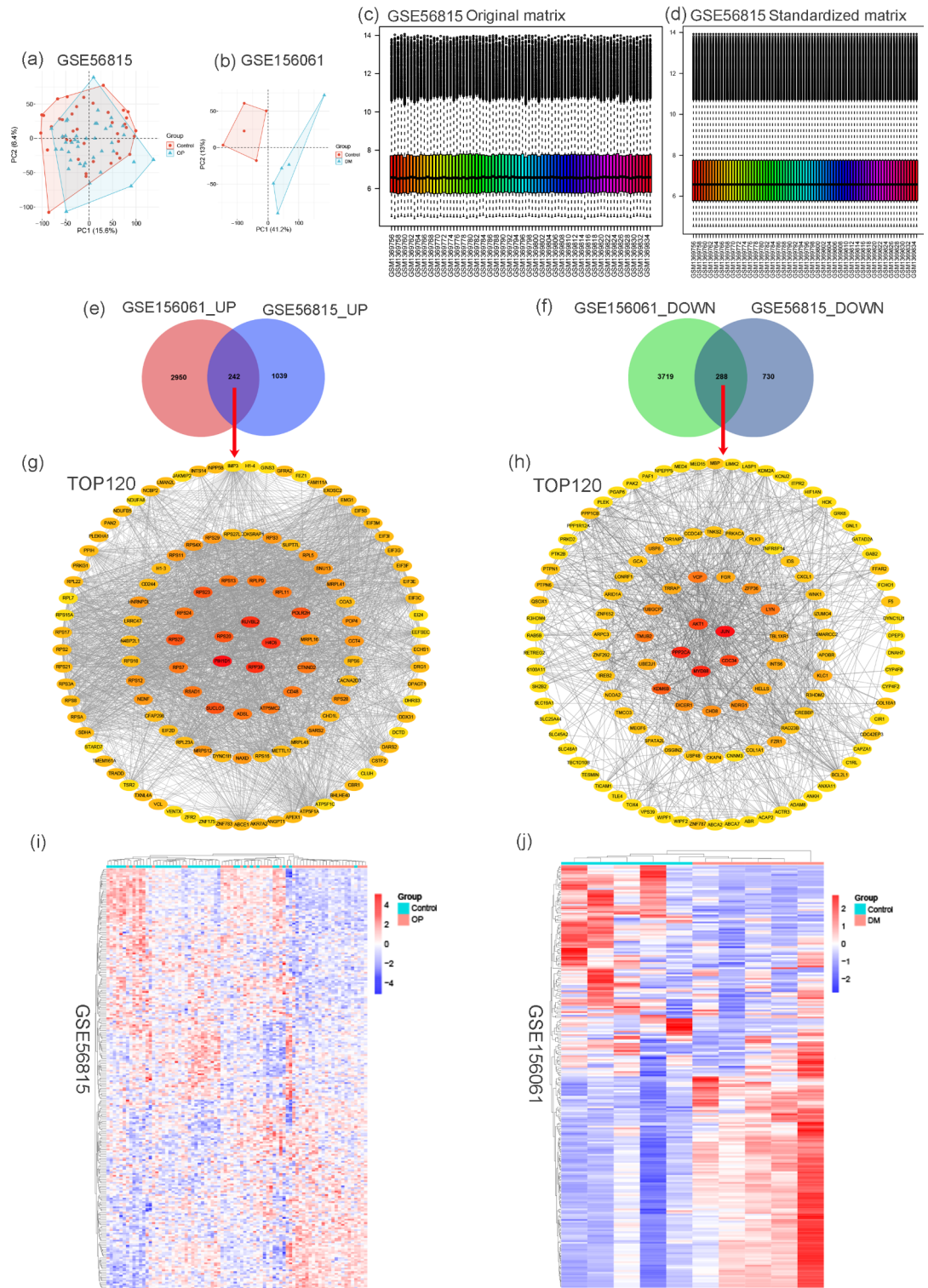


Fig. 2. Screening of differentially expressed genes (DEGs) from public datasets. (a) GSE56815 principal component analysis. (b) GSE156061 principal component analysis. (c) GSE56815 raw matrix. (d) GSE56815 normalized matrix. (e) Intersection between DEGs upregulated in GSE156061 and DEGs upregulated in GSE56815. (f) Intersection between DEGs downregulated in GSE156061 and GSE56815. (g) The top 120 genes were chosen after screening the upregulated DEGs in Cytoscape using the bottleneck method. (h) The top 120 genes were selected after screening the downregulated DEGs in Cytoscape using the bottleneck method. (i) Top 240 genes (including upregulated and downregulated genes) in the GSE56815 expression heatmap. (j) Top 240 genes (including upregulated and downregulated genes) in the GSE156061 expression heatmap.

was used to search for upregulated and downregulated DEGs in Cytoscape; the top 120 genes are presented in Fig. 2g,h. Gene expression heatmaps of the top 240 genes are presented in Fig. 2i,j.

Gene ontology (GO) and Kyoto encyclopedia of genes and genomes (KEGG) analyses of DEGs and gene set enrichment analysis (GSEA) of datasets

The GO and KEGG analyses were conducted to determine the biological implications of the gene expression changes observed in our study. The GO analysis revealed that the top 120 upregulated genes were predominantly involved in translational initiation and co-translational proteins targeting the membrane. Concurrently, the KEGG pathway analysis indicated significant enrichment of these genes in oxidative physiology, ribosomes, and pathways pertinent to diabetic cardiomyopathy (Fig. 3a,b). Conversely, the top 120 downregulated genes were found to be mainly associated with the immune response-activating cell surface receptor signaling pathway through the GO analysis, while the KEGG pathway analysis underscored their abundance in the Wnt signaling pathway, Nuclear Factor kappa-light-chain-enhancer of activated B cells (NF- κ B) signaling system, and the AGE-RAGE signaling network, all of which are key players in diabetic complications (Fig. 3c,d).

The GSEA provided deeper insights. In GSE56815, oxidative phosphorylation, the IL5 pathway, tRNA aminoacylation, and type 1 DM were identified as positively regulated signaling pathways, whereas the IL18 signaling pathway, oxidative stress-induced senescence, apoptosis modulation and signaling, and apoptosis were negatively regulated (Fig. 3e,f). In GSE156061, mitochondrial tRNA aminoacylation and oxidative phosphorylation were positively regulated, whereas type 2 DM, IL4, TNF, Pi3k-Akt, and notably, the IL18 signaling pathway (Fig. 3g,h) were negatively regulated. The consistent identification of the IL18 signaling pathway and cellular processes related to apoptosis as negatively regulated entities across both datasets highlights their critical significance.

Processing of raw data and DEG cluster analysis based on the Mfuzz time series

Following matrix standardization, principal component analysis of the gene expression data showed good discrimination between the disease and control groups (Fig. 4a,b). In RNA-seq differential gene screening, 1880 DEGs were found in the DM group and 878 DEGs were found in the DMOP group (Fig. 4c,d). RNA sequencing divided genes into nine categories, and clusters 6 and 7 were selected for further analysis, as these showed either increased or decreased expression in the “Normal–DM–DMOP” models (Fig. 4e). The core genes PRKD2 and WIPF1 exhibited a declining trend of expression in the RNA-seq data, GSE56815 (OP), GSE156061 (DM), and cluster 7. LMAN2L exhibited an increasing trend of expression in the RNA-seq data, GSE56815 (OP), GSE156061 (DM), and cluster 7 (Fig. 4f–i). The expression of PRKD2, WIPF1, and LMAN2L in the RNA-seq data, GSE56815, and GSE156061 is summarized in Fig. 4j–l.

Immune cell filtration analysis

CIBERSORT was employed to analyze immune cell infiltration in DM, DMOP, and normal samples using RNA sequencing. We compared 22 immune cell types, as shown in box plots (Fig. 5a). Heatmaps (Fig. 5b) and bar maps (Fig. 5c) of immune cell infiltration were generated for each sample. These results revealed significantly reduced proportions of resting natural killer (NK) cells in DM and DMOP samples compared to normal samples ($P < 0.05$).

Receiver operating characteristic (ROC) curves of the core genes

ROC analysis was performed on three hub genes, and the results showed that the area under the curve of PRKD2, WIPF1, and LMAN2L was greater than or equal to 0.6 in all three datasets, indicating that these hub genes have good diagnostic value for diabetes and OP (Fig. 5d–f).

Screening core gene TFs and miRNAs based on bioinformatics

Next, we employed bioinformatic approaches to identify the TFs and miRNAs associated with the three core genes mentioned above. The TFs shared by the three genes were EP300, ERG, CBFb, CTCF, and BRD4. The top 20 miRNAs and TFs of these genes are shown in Fig. 6.

Screening for drugs that may increase or decrease core gene expression

Among the screened drugs, the most common was bisphenol A, which regulates the expression of all three core genes. Ethinyl estradiol regulates the expression of LMAN2L, whereas valproic acid regulates the expression of PRKD2 and WIPF1 (Table 1). Some drugs, such as folic acid, are commonly used clinically and may alter the expression of core genes when used to treat other diseases, potentially affecting the progression of DMOP.

Further cell model validation of the expression of PRKD2

RT-PCR was performed on the three core genes and the difference in PRKD2 expression was found to be the most significant (Fig. 7a,b). Consequently, PRKD2 was chosen for in-depth validation. Subsequent establishment of a cell model facilitated further investigation. Within this model, immunofluorescence staining revealed a significant augmentation in caspase-3 fluorescence intensity, concomitant with a marked reduction in BCL2 signal intensity across both the DM and DMOP groups (Fig. 7c–f). These observations were substantiated by western blot analysis, which demonstrated significant upregulation of caspase-3 and BAX expression, alongside notable downregulation of BCL2 and RUNX2 expression (Fig. 7g,h). Additionally, immunofluorescence staining showed a notable decrease in the PRKD2 fluorescence signal in both the DM and DMOP groups (Fig. 7i,j). This finding was further supported by western blot analysis, which indicated significant downregulation of PRKD2 (Fig. 7k,l), thereby underscoring the critical role of PRKD2 in the pathophysiological processes under investigation.

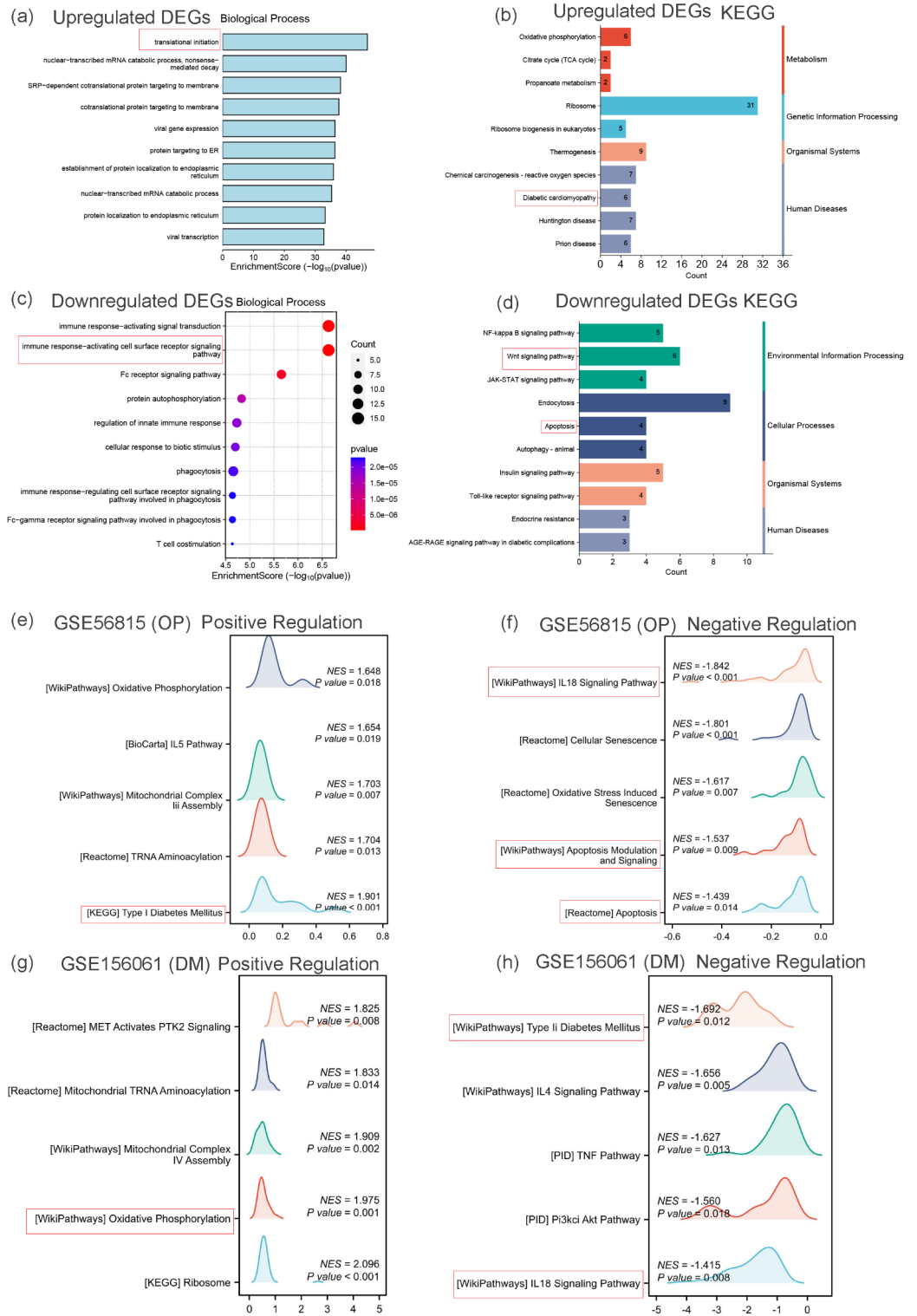


Fig. 3. GO and KEGG analyses and GSEA. **(a)** Biological processes of upregulated differentially expressed genes (DEGs). **(b)** KEGG analysis of upregulated DEGs. **(c)** Biological processes of downregulated DEGs. **(d)** KEGG analysis of downregulated DEGs. **(e)** Positively regulated signaling pathways in GSE56815. **(f)** Negatively regulated signaling pathways in GSE56815. **(g)** Positively regulated signaling pathways in GSE156061. **(h)** Negatively regulated signaling pathways in GSE156061. The pathways illustrated in this figure were based on information obtained from the Kyoto Encyclopedia of Genes and Genomes (KEGG) database (available at: www.kegg.jp/kegg/kegg1.html).

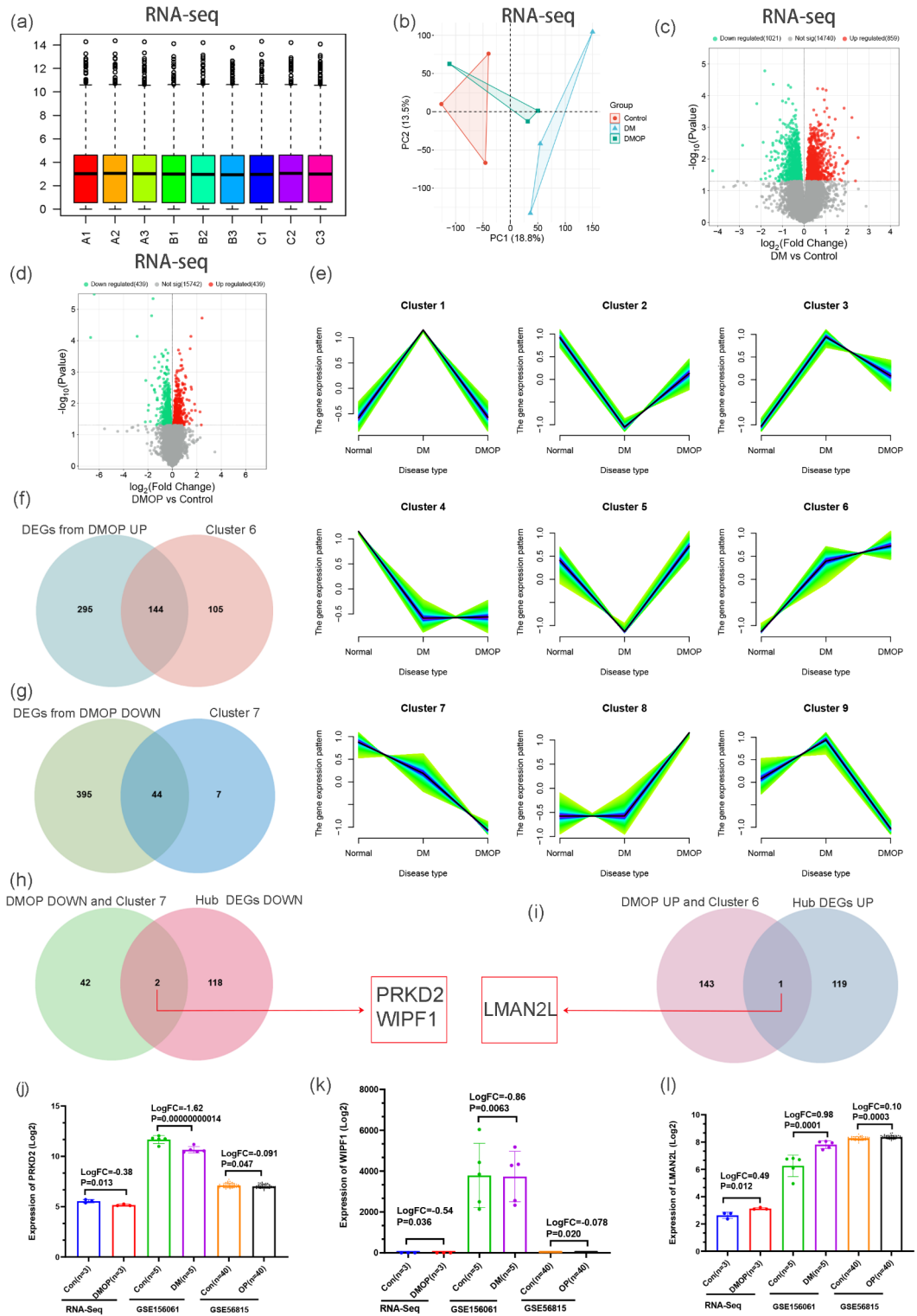


Fig. 4. RNA Sequencing data processing and screening of core differentially expressed genes. **(a)** Standardized data matrix. **(b)** RNA sequencing (RNA-seq) principal component analysis. **(c)** DM vs. control differential gene expression volcano map. **(d)** DMOP vs. control differential gene expression volcano map. **(e)** Performing Mfuzz clustering analysis on RNA-seq data. **(f)** Detecting differentially expressed genes (DEGs) in DMOP UP and cluster 6 (gradually rising in “Normal–DM–DMOP”). **(g)** Detection of DEGs in DMOP DOWN and cluster 7 (gradually declining in “Normal–DM–DMOP”). **(h)** Detection of DEGs in DMOP UP and cluster 6 and the top 120 hub DEGs in UP (from Cytoscape using the bottleneck method). **(i)** Detecting DEGs in DMOP DOWN and cluster 7 and the top 120 hub DEGs in DOWN (from Cytoscape using the bottleneck method). **(j)** Expression of PRKD2 in RNA-seq data, GSE56815, and GSE156061. **(k)** WIPF1 expression in RNA-seq data, GSE56815, and GSE156061. **(l)** Expression of LMAN2L in RNA-seq data, GSE56815, and GSE156061.

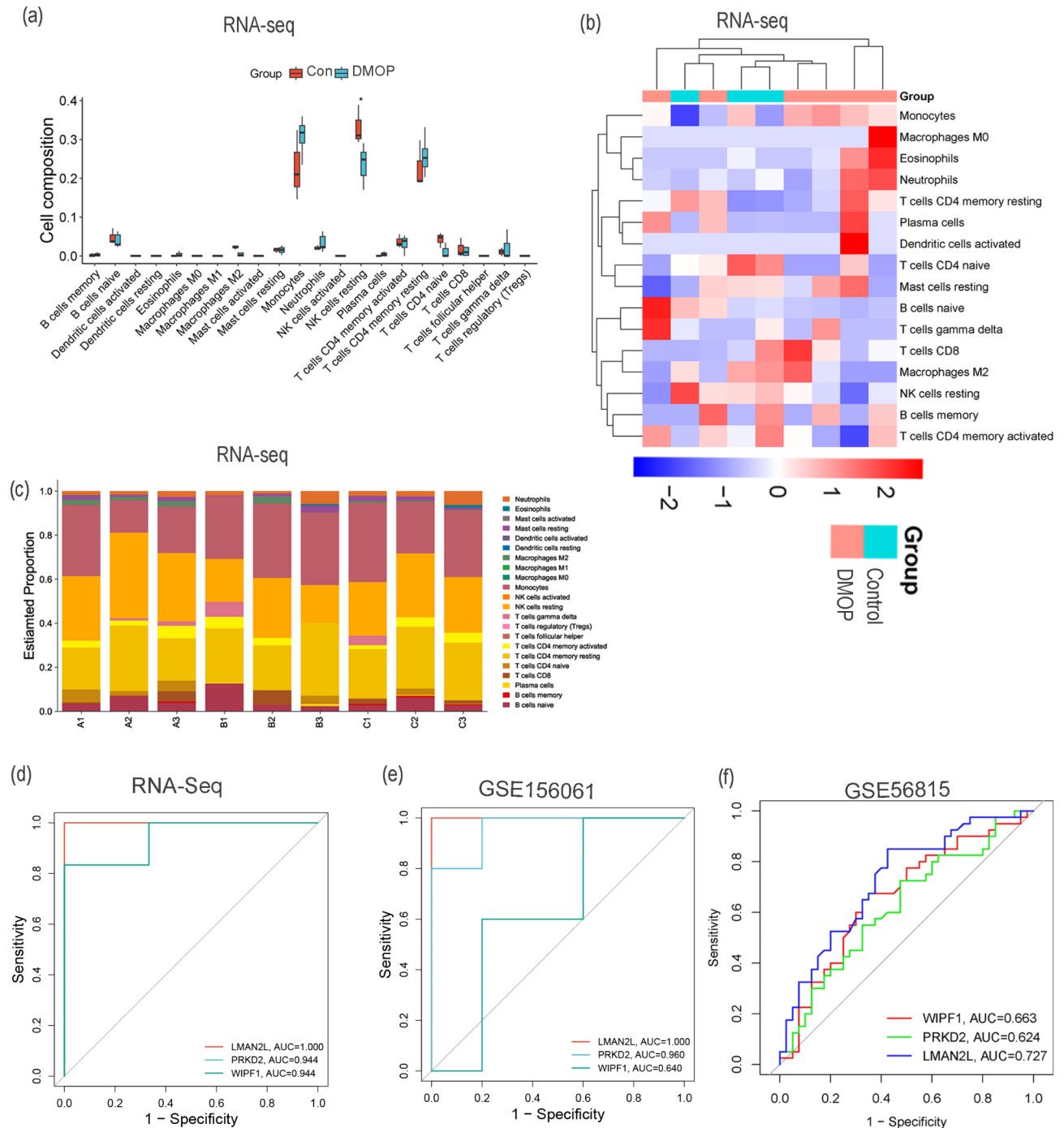


Fig. 5. Immune cell infiltration and ROC curve analysis. **(a)** Box plots illustrating the comparison of 22 immune cell types using RNA-seq. **(b)** Immune cell infiltration heatmap for each RNA-seq sample. **(c)** Immune cell infiltration bar map for each RNA-seq sample. **(d)** ROC curve of RNA-seq. **(e)** GSE156061 ROC curve. **(f)** GSE56815 ROC curve.

Further animal model validation of PRKD2 expression

To further validate the expression of PRKD2 *in vivo*, we established an animal model (Fig. 8a). Micro-CT analyses of both the DM and DMOP groups revealed significant bone deterioration compared with that in the control group (Fig. 8b). Moreover, both the DM and DMOP groups were characterized by a pronounced decrease in femoral volume; sparse and fragmented bone trabeculae; significant reductions in bone mineral density (BMD), bone volume/ total volume (BV/TV), and trabecular thickness (Tb.Th); and increase in bone surface area/ bone volume (BS/BV) and trabecular separation (Tb.Sp) (Fig. 8c). Concurrently, Hematoxylin and eosin (H&E) staining revealed substantial alterations in bone architecture within these groups. Notably, there was a significant reduction in trabecular number, with the remaining trabeculae appearing thinner and more

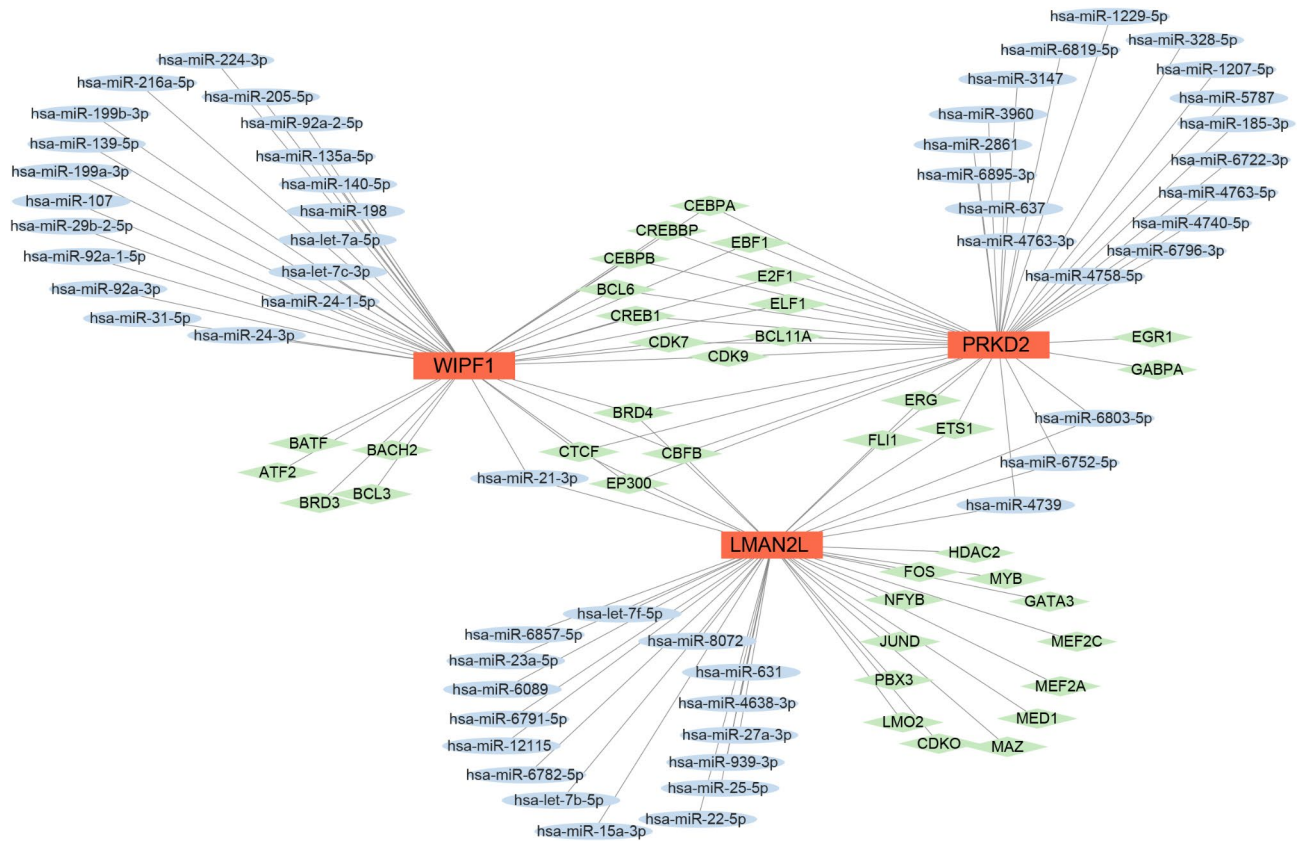


Fig. 6. Transcription factor and miRNA network regulation diagrams of core genes.

Name	Target	Interaction	Chemical formula
Bisphenol A	PRKD2	Bisphenol A results in decreased expression of PRKD2 mRNA	C15H16O2
Coumarin	PRKD2	Coumarin results in decreased phosphorylation of PRKD2 protein	C9H6O2
Estradiol	PRKD2	Estradiol results in increased expression of PRKD2 mRNA	C18H24O2
Valproic acid	PRKD2	Valproic acid results in increased expression of PRKD2 mRNA	C8H16O2
Zinc acetate	PRKD2	Zinc acetate results in decreased expression of PRKD2 mRNA	C4H6O4Zn
Bisphenol A	WIPF1	Bisphenol A results in increased expression of WIPF1 mRNA	C15H16O2
Estradiol	WIPF1	Estradiol results in decreased expression of WIPF1 mRNA	C18H24O2
Folic acid	WIPF1	Folic acid results in decreased expression of WIPF1 mRNA	C19H19N7O6
Triptonide	WIPF1	Triptonide results in decreased expression of WIPF1 mRNA	C20H22O6
Valproic acid	WIPF1	Valproic acid results in increased expression of WIPF1 mRNA	C8H16O2
Bisphenol A	LMAN2L	Bisphenol A results in decreased expression of LMAN2L mRNA	C15H16O2
Triptonide	LMAN2L	Triptonide results in increased expression of LMAN2L mRNA	C20H22O6
Ethinyl estradiol	LMAN2L	Ethinyl estradiol results in increased expression of LMAN2L mRNA	C20H24O2
Cisplatin	LMAN2L	Cisplatin results in increased expression of LMAN2L mRNA	Cl2H6N2Pt
Fenretinide	LMAN2L	Fenretinide results in decreased expression of LMAN2L mRNA	C26H33NO2

Table 1. Targeted drugs that increase or decrease core gene expression.

fragile (Fig. 8d). Additionally, Masson’s trichrome staining indicated a decrease in collagen fibers, an essential component of the bone matrix (Fig. 8d,e), which was further supported by diminished intensity of Alizarin Red staining, suggesting a reduction in calcification activity (Fig. 8d,f). Von Kossa staining also revealed a decrease in bone mineralization, further supporting a decline in bone quality (Fig. 8d,g).

Collectively, these results underscore the significant effect of diabetes and OP on the distal femur of mouse models, demonstrating a synergistic effect that exacerbates the deterioration of bone quality and integrity. Moreover, immunofluorescence staining showed a significant reduction in PRKD2 fluorescence intensity in both the DM and DMOP groups, consistent with our cellular model findings (Fig. 8h,i). This comprehensive

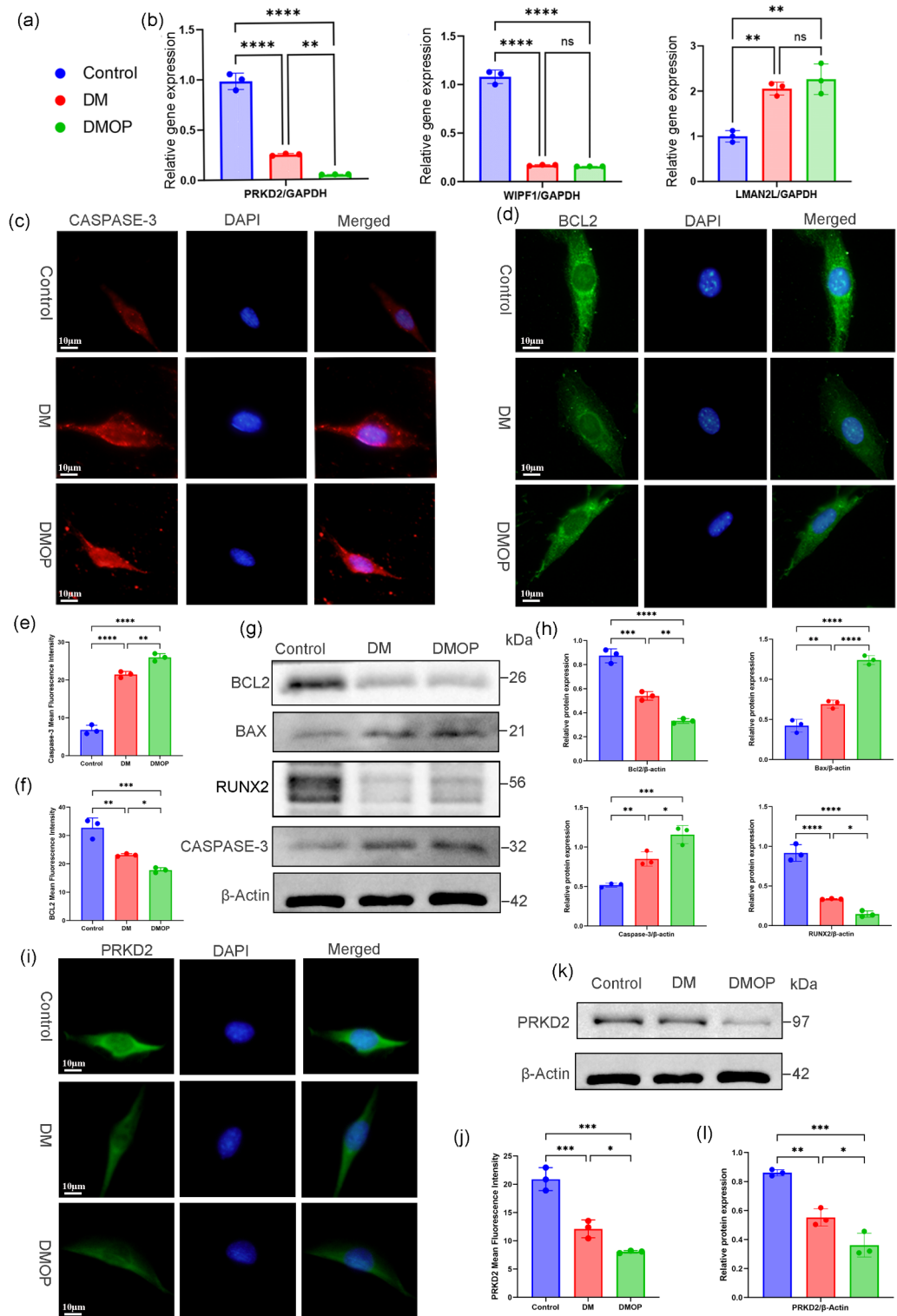


Fig. 7. Validation of PRKD2 expression in cells. **(a)** Comparison among study groups: control (blue), diabetes mellitus (DM, red), and diabetes mellitus with osteoporosis (DMOP, green). **(b)** qRT-PCR validation of PRKD2, WIPF1, and LMAN2L in the control, DM, and DMOP groups. **(c–f)** Immunofluorescence and quantitative fluorescence analyses of caspase-3 and BCL2. **(g,h)** Western blot and quantitative analyses were used to measure BAX, BCL2, RUNX2, and caspase-3 expression in MC3T3-E1 cells. **(i,j)** Immunofluorescence and quantitative fluorescence analyses of PRKD2. **(k,l)** Western blot and quantitative analyses were used to measure PRKD2 expression in MC3T3-E1 cells (Original blots are presented in Supplementary material 1).

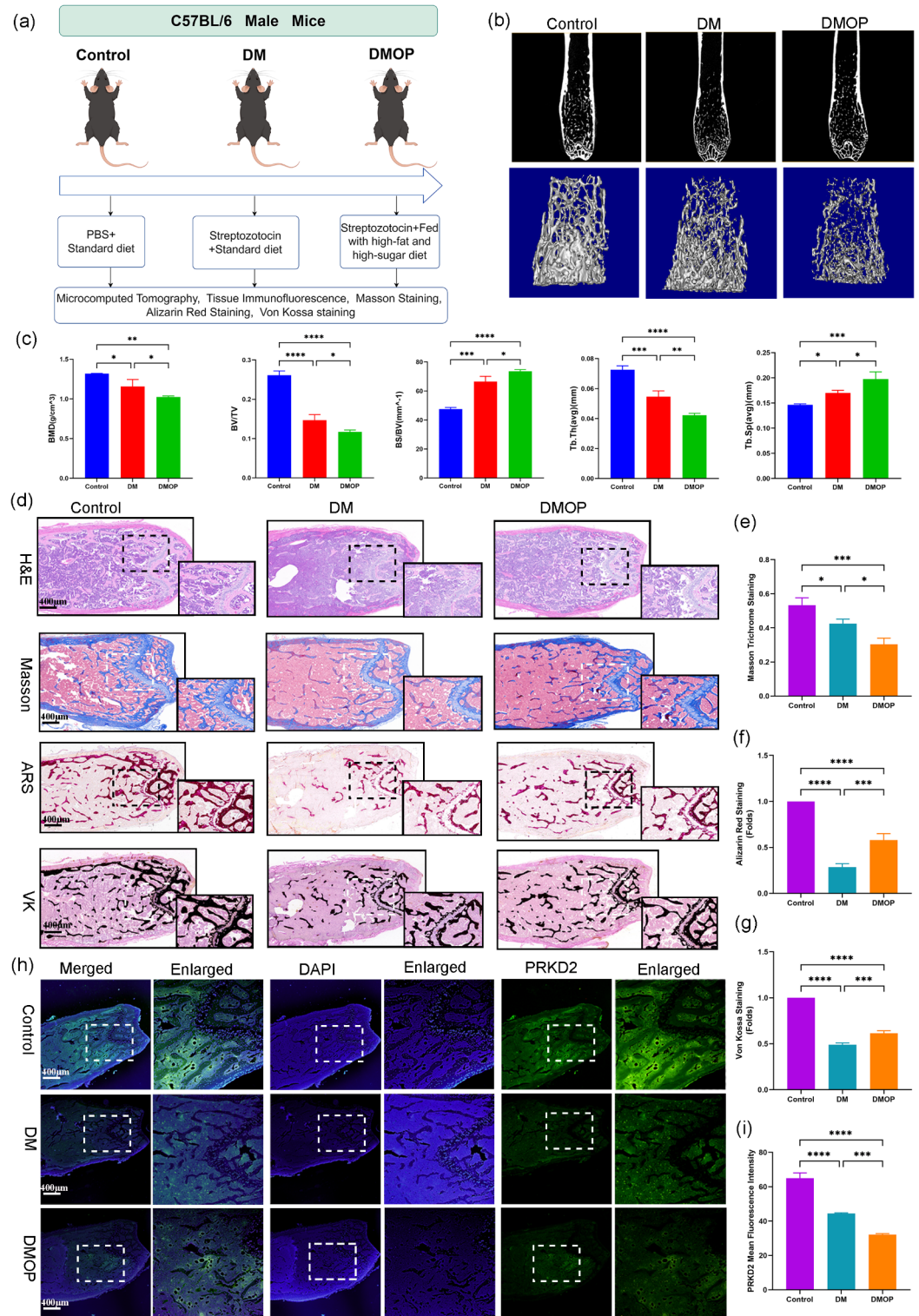


Fig. 8. Animal model validation of PRKD2 expression. **(a)** Flowchart of in vivo experiments. **(b)** Representative micro-CT reconstruction images of the distal femurs. **(c)** Quantitative assessment of the distal femur through micro-CT encompassed analysis of the bone mineral density (BMD, mg/cm³), percentage bone volume (BV/TV, %), bone surface area to bone volume ratio (BS/BV, 1/mm), trabecular thickness (Tb.Th, μm), and separation between trabeculae (Tb.Sp, μm). **(d–g)** H&E, Masson’s trichrome, Alizarin Red (ARS), and Von Kossa (VK) staining and their respective quantitative analyses were employed to assess the control, DM, and DMOP groups. **(h,i)** Immunofluorescence and quantitative fluorescence analyses of PRKD2 in the distal femurs of mice were performed. Results are expressed as mean ± SD; significance levels are denoted as **P* < 0.05, ***P* < 0.01, and ****P* < 0.001, determined using the ANOVA and further analyzed with Tukey’s post-hoc test.

analysis highlights the critical role of PRKD2 in the pathological processes affecting bone health in the context of diabetes and OP.

Discussion

This study focused on the interplay between type 2 DM and OP, two prevalent conditions with substantial public health implications. By applying the Mfuzz time-series gene clustering method and transcriptome sequencing, we systematically identified gene expression clusters that reflect the transition from a normal state to DM and, subsequently, to a DMOP state. This analysis enabled us to define the “Normal–DM–DMOP” progression pattern, highlighting the dynamic changes in gene activity across different disease stages. Among the identified genes, protein kinase D2 (PRKD2) is notable owing to its significant downregulation and possible role in the pathogenesis of both conditions.

PRKD2, a serine/threonine kinase, plays a pivotal role in various cellular processes, including cell migration, differentiation, and apoptosis^{16–19}. Structurally, PRKD2 contains a pleckstrin homology domain, which is crucial for its recruitment to cell membranes and activation in response to signaling molecules²⁰. Reportedly, PRKD2 deficiency triggers hyperinsulinemia and metabolic disorders in mice, which is consistent with the results of human peripheral monocyte sequencing obtained in the present study²¹.

One key aim of this study was to identify and validate key genes, specifically, *WIPF1* and *LMAN2L*, which play important roles in the pathogenesis of both DM and OP. In previous studies, *WIPF1* was considered to be associated with gastric cancer²² and epilepsy²³. In the present study, three databases were used to verify that this gene may also be related to DMOP; however, additional research is warranted for confirmation. A previous study²⁴ analyzed the genetic association of *LMAN2L* in schizophrenia and bipolar disorder through Mendelian randomization. All three databases revealed that this gene may be related to DMOP, and future research should continue to study the expression of *LMAN2L* in patients with diabetes and schizophrenia.

In this study, these core genes were implicated in various signaling pathways, as identified through the GO and KEGG analyses, including the ATPase complex, animal insulin signaling pathway, and notably, the Wnt signaling pathway. The Wnt pathway, pivotal for bone formation and glucose metabolism^{25–28}, has been implicated in the regulation of bone density and the manifestation of diabetic complications²⁹, thus underscoring the significance of PRKD2 downregulation.

The IL-18 signaling pathway was significantly enriched in both diabetes and OP datasets via the GSEA analysis. IL-18, a pro-inflammatory cytokine, has been implicated in the regulation of immune responses and inflammation³⁰. Its elevated levels in diabetes enhance inflammation, damaging pancreatic β -cells and impairing insulin function, while worsening diabetes-related complications^{31–33}. In OP, IL-18 promotes osteoclast activity and inhibits osteoblast function, exacerbating bone loss^{34,35}. The interplay between diabetes and OP involves the IL-18 pathway, where increased IL-18 levels in diabetes not only aggravate inflammation but also negatively affects bone metabolism, heightening OP risk³⁶. Conversely, OP can influence diabetes progression through its effects on inflammation and pancreatic function. Targeting the IL-18 signaling pathway offers a promising approach for treating both conditions. Future research should aim to clarify the specific roles of IL-18 in diabetes and OP to strengthen clinical treatment strategies.

The establishment of miRNA–mRNA–transcription factor (TF) networks for pivotal genes, including PRKD2, lays the foundation for deciphering regulatory mechanisms and developing novel intervention strategies. NK cells are essential for innate immune defense against tumors and pathogens, and the proportion of NK cells is significantly reduced in patients with DMOP. This reduction aligns with the changes observed in DM and OP individually and highlights the compounded effect on immune function when both conditions coexist. The decline in NK cell proportions in DMOP may result from shared chronic inflammation and DM-specific metabolic alterations, impairing NK cell function and survival³⁷. These findings emphasize the critical need for monitoring NK cell levels in DMOP management, suggesting that interventions to restore immune balance may improve patient outcomes.

To validate the significance of certain genes for diagnosis and therapy, we performed ROC curve analysis. This method quantitatively assessed the effectiveness of the genes as disease biomarkers through their sensitivity and specificity. In our search for therapeutic drugs, bisphenol A emerged as a prominent candidate, demonstrating a unique ability to regulate all three targeted genes. This observation highlights its significant role in potentially altering gene expression. By combining the regulatory effects of bisphenol A, ROC curve analysis results, and Comparative Toxicogenomics Database (CTD) results, we demonstrated the potential of the target genes in diagnosis and treatment and outlined a streamlined drug discovery process. Our findings deepen the understanding of genetic disease mechanisms and open new avenues for targeted and personalized therapies.

This study highlights the therapeutic potential of PRKD2 in DMOP by reporting its critical involvement in apoptosis and bone metabolism through both cellular and animal model validation. The observed downregulation of PRKD2 expression elucidates the complex interplay between bone health and glucose metabolism, advancing our understanding of DMOP beyond the separate considerations of DM or OP. This research provides new insights into the molecular mechanisms of DMOP, identifying PRKD2 as a pivotal, previously unexplored target, and underscores the importance of targeted therapeutic approaches in DMOP management. These findings not only affirm bioinformatic predictions but also establish a strong foundation for PRKD2 as a novel therapeutic target.

Although this study has yielded certain insights, it remains somewhat limited. Notably, a relatively small number of clinical samples was used. In addition to the modest sample size in the GSE156061 (DM) dataset, a relatively small sample size for RNA sequencing from volunteers was used. These small sample sizes may limit the broader applicability of our research findings. It is imperative that future research incorporate larger sample sizes to validate the findings reported herein and further investigate the clinical significance of PRKD2 in DMOP. Furthermore, studies on a larger scale would enhance our understanding of PRKD2's role in the pathogenesis of

DMOP, laying a more robust scientific groundwork for novel therapeutic approaches. Additionally, the molecular mechanisms through which PRKD2 influences the pathogenesis of DMOP warrant further exploration.

In conclusion, this study identified PRKD2 as a key molecule in the pathogenesis of DMOP, highlighting its therapeutic potential. Through Mfuzz time-series gene clustering and validation experiments, we demonstrated the critical role of PRKD2 in linking bone health and glucose metabolism. These findings validate previous bioinformatic predictions and pave the way for novel treatment strategies targeting PRKD2. Future efforts should aim to validate these findings in larger cohorts and further explore the mechanisms of PRKD2 to fully harness its therapeutic potential.

Methods

Data preprocessing and differential gene screening for DM and DMOP

Nine volunteers provided informed consent following the Ethics Committee standards (Lanzhou University Second Hospital, No. 2024 A-692). Peripheral venous blood (10 mL) was obtained from healthy volunteers ($n=3$) and volunteers with DM ($n=3$) or DMOP ($n=3$) at Lanzhou University Second Hospital. Peripheral blood mononuclear cells were extracted using the Ficoll Hypasque gradient (TBD, Tianjin, China), and monocytes were isolated via cell depletion using magnetic beads (Miltenyi Biotech, San Diego, CA, USA). Total RNA was isolated from monocytes using the AG RNAex Pro Reagent and subjected to strand-specific RNA sequencing on a HiSeq 2500 platform (Illumina, San Diego, CA, USA). Bulk RNA sequencing was performed. First, data processing and quality control were conducted in which the BWA algorithm filtered out low-quality regions, adapter sequences, ambiguous bases (N), and sequences under 60 bp, thus ensuring data integrity for further analysis. Quality metrics such as distribution, GC content, and base distribution were assessed pre- and post-filtering. HISAT2 aligned the cleaned data to the reference genome, producing BAM files and detailed alignment statistics to guarantee precision and sensitivity. Transcriptome assembly and expression analysis were conducted using StringTie, enabling the reconstruction of transcripts and quantification of gene expression. We employed FastQC and cutadapt for quality control, HISAT2 and SAMtools for alignment, StringTie and DESeq2 for assembly and expression analysis, and DESeq2 and bcftools for differential analysis, with R and Cytoscape for visualization.

The R (R Foundation for Statistical Computing, Vienna, Austria) “limma” package was used to perform differential gene expression analysis on the sequencing data, with $|\log_2FC| > 0$ and $P < 0.05$ used as screening criteria. Volcano plots based on the differential expression data were generated using the “ggplot2” package in R (version 4.2.1), and gene matrix heat maps were drawn using the R “ComplexHeatmap” package. The “VennDiagram” package in R was used to independently display the upregulated or downregulated intersecting genes in the form of a Wayne diagram. A flowchart of this method is shown in Fig. 1.

Mfuzz time-series gene clustering analysis

We used the “Mfuzz”¹⁵ R software package with the rule “Normal–DM–DMOP” to identify clusters of genes whose expression increased or decreased in DM and DMOP, as well as to extract cluster genes for further analysis.

External dataset validation

We analyzed the GSE156061 (DM) dataset, which included data from 5 healthy controls and 5 patients with diabetes, and the GSE56815 (OP) dataset, which included data from 40 patients with high and 40 with low hip BMD. Based on the sequencing data, the DEGs were intersected with the external dataset using a Wayne diagram online tool³⁸, and the relevant gene expression levels were plotted using GraphPad Prism 9 (GraphPad Software, San Diego, CA, USA).

Functional enrichment analysis of intersecting genes

We performed KEGG pathway enrichment analysis and GO annotation using the Metascape (metascape.org) web-based portal for comprehensive gene annotation and analysis resources³⁹. The GO analysis encompassed three categories: cellular component, molecular function, and biological process. The open-access online platform Bioinformatics (www.bioinformatics.com.cn) was used to generate a bubble chart for bioinformatic data analysis.

GSEA of GSE56815 (OP) and GSE156061 (DM)

GSEA identified significantly enriched gene sets and their changing expression trends. The enrichment analysis results were visualized using the ggplot2 package (version 3.4.4) within R (version 4.2.1). The default weighted enrichment statistical method was used to analyze the potential effect pathways of the core genes in the datasets GSE56815 (OP) and GSE156061 (DM). The absolute number of the normalized enrichment score $|(NES)| > 1$, false discovery rate (FDR) < 0.25 , and $P < 0.05$ were the filter criteria.

Immune cell infiltration analysis

Disease pathogenesis is typically studied by analyzing immune cell infiltration, which allows for the quantification of various immune cell proportions within a sample⁴⁰. To compare immune cell populations between healthy participants and patients with DM or DMOP, we applied this technique to RNA-seq data. Box plots were used to depict the immune cell distribution in the two sample groups. Variations in the percentage of immune cells were evaluated using the Wilcoxon rank-sum test. Statistical significance was set at $P < 0.05$. The image was generated using <https://www.bioinformatics.com.cn>, an online platform dedicated to data analysis and visualization, last accessed on 10 December 2024.

Potential drug prediction of core genes

The CTD (<http://ctdbase.org/>) is a comprehensive web-based drug prediction tool that manually selects, correlates, and organizes content on chemicals, genes, phenotypes, anatomy, diseases, taxa, and exposure from published literature to harmonize cross-species heterogeneous data on chemical exposures and their biological effects⁴¹. To examine possible pharmacological targets for the cross genes of DMOP, drug–gene relationships in CTD were explored and the top five medications were selected for each gene based on a reference list from high to low, with strong clinical application as the screening criterion.

ROC curves of the core genes

The core genes of the RNA-seq data of the diseased and normal tissues and the disease and control groups of the GSE56815 (OP) and GSE156061 (DM) datasets were extracted. ROC curves of the core genes were analyzed using the “pROC” package in R software, and the area under the ROC curve was calculated to evaluate the clinical efficacy of these core genes in predicting disease.

Construction of miRNA–mRNA–transcription factor networks for the core genes

The miRNAs of the core genes were predicted using miRWalk (<http://mirwalk.umh.uni-heidelberg.de>), which is a bioinformatics tool that predicts target genes and miRNA–gene pairings^{42,43}. To enhance prediction accuracy, we identified the top 20 miRNAs for further research based on their scores. The TFs of core genes were predicted using hTFtarget (<http://bioinfo.life.hust.edu.cn/hTFtarget>), which combined data on epigenetic modifications with massive human TF target resources (7190 ChIP-seq samples of 659 TFs and the high-confidence binding sites of 699 TFs) to predict precise TF target regulations⁴⁴, and screening criteria included choosing the top 20 TFs from blood sources for each gene. Cytoscape 3.9.1 (Boston, MA, USA) was used to visualize the miRNA–mRNA–TF regulatory network.

Experimental verification

Cell culture

The mouse MC3T3-E1 cell line was acquired from the Peking Union Medical College Cell Bank (Beijing, China). Fetal bovine serum (10%) and α -minimum essential medium α (α -MEM) (HyClone, Logan, UT, USA) were used to prepare cell media. The culture conditions were 37 °C and 5% CO₂.

Cell model

We established a DM group (α -MEM with 25.5 mM glucose [Targetmol, Boston, USA]) and a DMOP group (high fat and sugar content: α -MEM with 25.5 mM glucose and 1 mM free fatty acids, at a 1:2 ratio of palmitic acid to oleic acid).

Animal model

Mice in the control group received intraperitoneal injections of phosphate-buffered saline (PBS) and were maintained on a standard laboratory diet for 5 weeks. Mice in the DM group were administered intraperitoneal injections of streptozotocin (50 mg/kg) once daily for three consecutive days and were also fed a standard laboratory diet for 5 weeks. Mice in the DMOP group received the same treatment with streptozotocin (50 mg/kg, once daily for three consecutive days) but were continued on a high-fat, high-sugar diet for 5 weeks. Following the treatment period, the mice were anesthetized and euthanized, and femoral bone tissue samples were collected within 6 h.

Western blotting

RIPA buffer was used to extract total protein from cells and bone tissue samples. Following protein quantification, the protein was combined with loading buffer at a 1:3 ratio and heated at 100 °C for 10 min to denature the proteins. After SDS-PAGE separation, the proteins were transferred onto polyvinylidene fluoride (PVDF) membranes (Millipore, Shanghai, China) and incubated for 2 h at 4 °C in a blocking solution. The PVDF membranes were incubated with diluted PRKD2 (1:1000, Biodragon, China), caspase-3 (1:1000, Abmart, China), RUNX2 (1:1000, Abmart), BCL2 (1:1000, Abmart), BAX (1:4000, Proteintech Group, China), and β -actin (1:5000, Immunoway, Plano, USA) antibodies at 4 °C overnight. ImageJ (Version 1.54) was used to analyze the protein bands following exposure to an ECL system (Bio-Rad, Hercules, CA, USA).

Micro-CT analysis

Data acquisition was performed using the Venus Micro CT system (Model: VNC-102, PINGSENG SCIENTIFIC, China), with Cruiser software utilized for data collection, Recon software for image reconstruction, and Avatar software for image display and application. The distal femur was extracted from each group of mice and subjected to ex vivo scanning. To assess the microstructure of the distal femur, we measured the trabecular bone volume fraction/total volume (BV/TV, %), bone surface area/bone volume (BS/BV, 1/mm), trabecular thickness (Tb.Th, μ m), and trabecular separation (Tb.Sp, μ m). Additionally, the BMD (g/cm³) was estimated.

RNA isolation and qPCR examination

Total RNA was isolated from tissues or cells using TRIzol (TaKaRa, Japan). Reverse transcription and target gene amplification were performed using the Preaugmentation[®] RT Master Mix Kit (TaKaRa) and TB Green PCR Master Mix Reagent. Relative amounts of mRNA were determined using an LC96 PCR system. GAPDH was used as an endogenous control for normalization. Gene expression levels were determined using the 2^{− $\Delta\Delta$ Ct} method⁴⁵. The sequences listed in Table 2 were developed and synthesized by Tsingke Biotechnology Co., Ltd. (Beijing, China).

Gene	Primer	Primer sequence
LMAN2L	F(5'→3')	GAACAAGCAGTTCTTCGCTATGG
LMAN2L	R(5'→3')	ACAAGGCACCCTGTTACTTTG
PRKD2	F(5'→3')	GGGGTCTCCTTCCATATCCAG
PRKD2	R(5'→3')	CACGATAGAACAGGCTAGTTGC
WIPF1	F(5'→3')	ACATTGCACTCGCTAACACT
WIPF1	R(5'→3')	GTCATTGGTGACCGTCTTCTTTA
GAPDH	F(5'→3')	AGGTCGGTGTGAACGGATTTG
GAPDH	R(5'→3')	GGGGTCGTTGATGGCAACA

Table 2. Primer sequences for qRT-PCR.

Hematoxylin and eosin (H&E) staining

Femur specimens were fixed in 4% paraformaldehyde for 24 h and then decalcified using 10% ethylenediaminetetraacetic acid for 21 days. After embedding in paraffin, the samples were sectioned to a thickness of 4 μm . The sections were stained with a H&E staining kit (Solarbio, Beijing, China), and bone morphology was examined using a light microscope (Olympus, Tokyo, Japan).

Immunofluorescence

Cells were initially fixed with 4% paraformaldehyde solution for 30 min, followed by a 25-min Triton treatment to enhance permeability. Then, a 1-h blockade with 5% goat serum was established, and the cells were rinsed with PBS. Both cells and tissue sections were then incubated with a primary antibody diluted in PBS (1:300) against PRKD2 overnight at 4 °C. After thorough washing, the samples were coated with a goat anti-rabbit IgG fluorescent secondary antibody (SA00013-2; Proteintech) diluted in PBS (1:300) and finally sealed with a solution containing 4',6-diamidino-2-phenylindole. Imaging and inspection of cells and tissue sections were performed using a camera and fluorescence microscope (Olympus, Tokyo, Japan).

Von Kossa staining

Initially, tissue sections were deparaffinized and immersed in water, followed by a 60-min exposure to Von Kossa's silver solution under intense illumination. Subsequently, the specimens were subjected to a 2-min treatment with a hypo solution. After a thorough dehydration process, the sections were encapsulated in a clear, neutral resin, facilitating microscopic examination and imaging.

Masson's trichrome staining

The preparation of femoral tissue slices involved dewaxing and rehydration. Following the protocol provided by the manufacturer, the slices were initially immersed in an iron hematoxylin solution for 5–10 min. A rapid differentiation process was then initiated using acidic ethanol for 8 s, after which the slices were thoroughly rinsed with water. Next, Masson's blue solution was applied to the slices for 5 min, followed by another rinse. A 1-min treatment with phosphomolybdic acid solution was then performed. The post-staining procedure encompassed microscopic evaluation, systematic dehydration, and encapsulation in neutral resin after ensuring transparency with xylene. Finally, microscopic examination and documentation were performed.

Alizarin red staining

Following the manufacturer's instructions (Solarbio, Beijing, China), the paraffin-embedded femoral tissue sections were initially dewaxed with water and then stained with Alizarin Red staining for 20 min. After staining, the sections were rinsed in distilled water, dehydrated in a series of alcohols of ascending concentration, cleared in xylene, and finally embedded in neutral resin. Microscopic examination and imaging of the stained samples were performed.

Statistical analysis

The results are presented as mean \pm standard deviation of three replicate experiments. The data were statistically analyzed using GraphPad Prism version 9.0 and SPSS 25.0, with some data visualized using R. Spearman correlation coefficients were used to calculate the correlations between variables, with a two-tailed $P < 0.05$ indicating statistical significance.

Data availability

The data underpinning the findings of this study can be found in the NCBI GEO database (<https://www.ncbi.nlm.nih.gov/geo>), with the accession codes GSE156061 and GSE56815. The RNA sequencing data used in this study have been uploaded as Supplementary Material 2. For enhanced reproducibility, we've provided the full data analysis code, including software details and usage instructions, in Supplementary Material 3.

Received: 18 November 2024; Accepted: 4 February 2025

Published online: 08 February 2025

References

- Yang, T. et al. An update on chronic complications of diabetes mellitus: from molecular mechanisms to therapeutic strategies with a focus on metabolic memory. *Mol. Med. (Cambridge Mass)* **30**, 71. <https://doi.org/10.1186/s10020-024-00824-9> (2024).
- Yu, M. G. et al. Protective factors and the pathogenesis of complications in diabetes. *Endocr. Rev.* **45**, 227–252. <https://doi.org/10.1210/edrv/bnad030> (2024).
- Wang, Y. et al. Trends of clinical parameters and incidences of diabetes mellitus complications among patients with type 2 diabetes mellitus in Hong Kong, 2010–2019: a retrospective cohort study. *EClinicalMedicine* **60**, 101999. <https://doi.org/10.1016/j.eclinm.2023.101999> (2023).
- Chen, S., Chen, L. & Jiang, H. Integrated bioinformatics and clinical correlation analysis of key genes, pathways, and potential therapeutic agents related to diabetic nephropathy. *Dis. Markers* **2022** (9204201). <https://doi.org/10.1155/2022/9204201> (2022).
- Wu, Y. et al. Impact of healthy lifestyle on the risk of type 2 diabetes mellitus in southwest China: a prospective cohort study. *J. Diabetes Invest.* **13**, 2091–2100. <https://doi.org/10.1111/jdi.13909> (2022).
- Armas, L. A. & Recker, R. R. Pathophysiology of osteoporosis: new mechanistic insights. *Endocrinol. Metab. Clin. North Am.* **41**, 475–486. <https://doi.org/10.1016/j.ecl.2012.04.006> (2012).
- Teng, Y. et al. What is the maximum tibial tunnel angle for transtibial PCL reconstruction? A comparison based on virtual radiographs, CT images, and 3D knee models. *Clin. Orthop. Relat.* **480**, 918–928 (2022).
- Ma, C., Yu, R., Li, J., Chao, J. & Liu, P. Targeting proteostasis network in osteoporosis: pathological mechanisms and therapeutic implications. *Ageing Res. Rev.* **90**, 102024. <https://doi.org/10.1016/j.arr.2023.102024> (2023).
- Song, P. et al. Canagliflozin promotes osteoblastic MC3T3-E1 differentiation via AMPK/RUNX2 and improves bone microarchitecture in type 2 diabetic mice. *Front. Endocrinol.* **13**, 1081039. <https://doi.org/10.3389/fendo.2022.1081039> (2022).
- Sun, D. et al. Enhancement of glycolysis-dependent DNA repair regulated by FOXO1 knockdown via PFKFB3 attenuates hyperglycemia-induced endothelial oxidative stress injury. *Redox Biol.* **59**, 102589. <https://doi.org/10.1016/j.redox.2022.102589> (2023).
- Behl, T. et al. Natural and synthetic agents targeting reactive carbonyl species against metabolic syndrome. *Molecules (Basel Switzerland)* **27** <https://doi.org/10.3390/molecules27051583> (2022).
- Futschik, M. E. & Carlisle, B. Noise-robust soft clustering of gene expression time-course data. *J. Bioinform. Comput. Biol.* **3**, 965–988. <https://doi.org/10.1142/s0219720005001375> (2005).
- Kumar, L. & M. E. F. Mfuzz: a software package for soft clustering of microarray data. *Bioinformatics* **2**, 5–7. <https://doi.org/10.6026/97320630002005> (2007).
- D'Haeseleer, P. How does gene expression clustering work? *Nat. Biotechnol.* **23**, 1499–1501. <https://doi.org/10.1038/nbt1205-1499> (2005).
- Kim, S. Y., Lee, J. W. & Bae, J. S. Effect of data normalization on fuzzy clustering of DNA microarray data. *BMC Bioinform.* **7**, 134. <https://doi.org/10.1186/1471-2105-7-134> (2006).
- Misawa, T. et al. Mutual inhibition between Prkd2 and Bcl6 controls T follicular helper cell differentiation. *Sci. Immunol.* **5** <https://doi.org/10.1126/sciimmunol.aaz0085> (2020).
- Yang, Z. F. et al. GABP transcription factor is required for development of chronic myelogenous leukemia via its control of PRKD2. *Proc. Natl. Acad. Sci. U. S. A.* **110**, 2312–2317. <https://doi.org/10.1073/pnas.1212904110> (2013).
- Fan, Y. et al. HAX1-dependent control of mitochondrial proteostasis governs neutrophil granulocyte differentiation. *J. Clin. Invest.* **132** <https://doi.org/10.1172/jci153153> (2022).
- Bernhart, E. et al. Protein kinase D2 regulates migration and invasion of U87MG glioblastoma cells in vitro. *Exp. Cell Res.* **319**, 2037–2048. <https://doi.org/10.1016/j.yexcr.2013.03.029> (2013).
- Miao, B. et al. Small molecule inhibition of phosphatidylinositol-3,4,5-triphosphate (PIP3) binding to pleckstrin homology domains. *Proc. Natl. Acad. Sci. U. S. A.* **107**, 20126–20131. <https://doi.org/10.1073/pnas.1004522107> (2010).
- Xiao, Y. et al. Deficiency of PRKD2 triggers hyperinsulinemia and metabolic disorders. *Nat. Commun.* **9**, 2015. <https://doi.org/10.1038/s41467-018-04352-z> (2018).
- Su, F. et al. WIPF1 promotes gastric cancer progression by regulating PI3K/Akt signaling in a myocardin-dependent manner. *iScience* **26**, 108273. <https://doi.org/10.1016/j.isci.2023.108273> (2023).
- Lu, M., Feng, R., Zhang, C., Xiao, Y. & Yin, C. Identifying novel drug targets for epilepsy through a brain transcriptome-wide association study and protein-wide association study with chemical-gene-interaction analysis. *Mol. Neurobiol.* **60**, 5055–5066. <https://doi.org/10.1007/s12035-023-03382-z> (2023).
- Lim, C. H. et al. Genetic association of LMAN2L gene in schizophrenia and bipolar disorder and its interaction with ANK3 gene polymorphism. *Prog. Neuro Psychopharmacol. Biol. Psychiatry* **54**, 157–162. <https://doi.org/10.1016/j.pnpbp.2014.05.017> (2014).
- Shahnazari, M., Yao, W., Corr, M. & Lane, N. E. Targeting the wnt signaling pathway to augment bone formation. *Curr. Osteoporos. Rep.* **6**, 142–148. <https://doi.org/10.1007/s11914-008-0025-5> (2008).
- Kim, J. H. et al. Wnt signaling in bone formation and its therapeutic potential for bone diseases. *Ther. Adv. Musculoskelet. Dis.* **5**, 13–31. <https://doi.org/10.1177/1759720x12466608> (2013).
- Chen, Y. & Alman, B. A. Wnt pathway, an essential role in bone regeneration. *J. Cell. Biochem.* **106**, 353–362. <https://doi.org/10.1002/jcb.22020> (2009).
- Jin, T. The WNT signalling pathway and diabetes mellitus. *Diabetologia* **51**, 1771–1780. <https://doi.org/10.1007/s00125-008-1084-y> (2008).
- Gassel, L. C. et al. Dysregulation of wnt signaling in bone of type 2 diabetes mellitus and diabetic charcot arthropathy. *BMC Musculoskelet. Disord.* **23** <https://doi.org/10.1186/s12891-022-05314-9> (2022).
- Lorey, S. L., Huang, Y. C. & Sharma, V. Constitutive expression of interleukin-18 and interleukin-18 receptor mRNA in tumour derived human B-cell lines. *Clin. Exp. Immunol.* **136**, 456–462. <https://doi.org/10.1111/j.1365-2249.2004.02465.x> (2004).
- Gui, R. et al. Deciphering interleukin-18 in diabetes and its complications: Biological features, mechanisms, and therapeutic perspectives. *Obes. Rev. Off. J. Int. Assoc. Study Obes.* **25**, e13818. <https://doi.org/10.1111/obr.13818> (2024).
- Sabuncu, T., Eren, M. A., Tabur, S., Dag, O. F. & Boduroglu, O. High serum concentration of interleukin-18 in diabetic patients with foot ulcers. *J. Am. Podiatr. Med. Assoc.* **104**, 222–226. <https://doi.org/10.7547/0003-0538-104.3.222> (2014).
- Jiang, Y., Zhou, L. & Yao, L. Serum levels of interleukin-18 in diabetic retinopathy patients: a meta-analysis. *Eur. J. Ophthalmol.* **33**, 2259–2266. <https://doi.org/10.1177/11206721231163900> (2023).
- De Martinis, M. et al. Alarmins in osteoporosis, RAGE, IL-1, and IL-33 pathways: a literature review. *Medicina (Kaunas Lithuania)* **56** <https://doi.org/10.3390/medicina56030138> (2020).
- Lee, M. & Partridge, N. C. Parathyroid hormone signaling in bone and kidney. *Curr. Opin. Nephrol. Hypertens.* **18**, 298–302. <https://doi.org/10.1097/MNH.0b013e32832c2264> (2009).
- An, Y. et al. Activation of ROS/MAPKs/NF-κB/NLRP3 and inhibition of efferocytosis in osteoclast-mediated diabetic osteoporosis. *FASEB J. Off. Publ. Fed. Am. Soc. Exp. Biol.* **33**, 12515–12527. <https://doi.org/10.1096/fj.201802805RR> (2019).
- Yoon Kim, D. & Kwon Lee, J. Type 1 and 2 diabetes are associated with reduced natural killer cell cytotoxicity. *Cell. Immunol.* **379**, 104578. <https://doi.org/10.1016/j.cellimm.2022.104578> (2022).
- Bardou, P., Mariette, J., Escudié, F., Djemiel, C. & Klopp, C. Jvenn: an interactive Venn diagram viewer. *BMC Bioinform.* **15**, 293. <https://doi.org/10.1186/1471-2105-15-293> (2014).
- Zhou, Y. et al. Metascape provides a biologist-oriented resource for the analysis of systems-level datasets. *Nat. Commun.* **10**, 1523. <https://doi.org/10.1038/s41467-019-09234-6> (2019).

40. Newman, A. M. et al. Robust enumeration of cell subsets from tissue expression profiles. *Nat. Methods* **12**, 453–457. <https://doi.org/10.1038/nmeth.3337> (2015).
41. Davis, A. P. et al. Comparative toxicogenomics database (CTD): update 2023. *Nucleic Acids Res.* **51**, D1257–d1262. <https://doi.org/10.1093/nar/gkac833> (2023).
42. Sticht, C., De La Torre, C., Parveen, A., Gretz, N. & miRWalk An online resource for prediction of microRNA binding sites. *PLoS ONE* **13**, e0206239. <https://doi.org/10.1371/journal.pone.0206239> (2018).
43. Muñoz, E. R. et al. Effects of purposeful soccer heading on circulating small extracellular vesicle concentration and cargo. *J. Sport Health Sci.* **10**, 122–130. <https://doi.org/10.1016/j.jshs.2020.11.006> (2021).
44. Zhang, Q. et al. hTFtarget: a comprehensive database for regulations of human transcription factors and their targets. *Genom. Proteom. Bioinform.* **18**, 120–128. <https://doi.org/10.1016/j.gpb.2019.09.006> (2020).
45. Livak, K. J. & Schmittgen, T. D. Analysis of relative gene expression data using real-time quantitative PCR and the 2(-Delta Delta C(T)) method. *Methods (San Diego California)* **25**, 402–408. <https://doi.org/10.1006/meth.2001.1262> (2001).

Acknowledgements

We sincerely express our gratitude to Bin Geng for his invaluable guidance and support, and to the Second Hospital of Lanzhou University for providing the necessary facilities for our research.

Author contributions

RC, CY, and HX were co-first authors who contributed equally to this work. RC, CY, and HX conceived and designed the study and wrote the paper. FY, AY, BP, CC, and BG consulted the literature, and acquired and analyzed the data. YX contributed to the design of the study and the critical revision of the manuscript for important intellectual content. All authors contributed to the manuscript and approved the submitted version.

Funding

This work was supported by The National Natural Science Foundation of China (Grant numbers 82060405 and 82360436); the Lanzhou Science and Technology Plan Program (Grant number 2021-RC-102); the Natural Science Foundation of Gansu Province (Grant numbers 22JR5RA943, 22JR5RA956, and 23JRRA1500); and the Cuiying Scientific and Technological Innovation Program of Lanzhou University Second Hospital (Grant number CY2021-MS-A07 and CY2022-MS-A19).

Declarations

Competing interests

The authors declare no competing interests.

Ethics approval

This study was designed and conducted to uphold the highest ethical standards for research involving both human participants and animals. In alignment with the ethical principles outlined in the 1964 Declaration of Helsinki and its subsequent amendments, we obtained ethical approval for our research involving human participants from the Institutional Review Board (IRB) of Lanzhou University Second Hospital, formally known as the Ethics Committee of Lanzhou University Second Hospital, under the approval number 2024 A-692. For research involving animals, we strictly adhered to the guidelines set forth by the Institutional Animal Care and Use Committee (IACUC) of Lanzhou University Second Hospital, formally known as the Animal Ethics Committee of Lanzhou University Second Hospital, which approved our experimental protocols under the approval number D2024-632. We took utmost care to ensure animal welfare throughout the study. Animals were anesthetized and euthanized using intraperitoneal injections of pentobarbital, with dosages calculated based on body weight to guarantee a rapid and painless procedure. All experimental protocols involving human participants were approved by the IRB of Lanzhou University Second Hospital. All procedures involving animals were performed in strict compliance with the guidelines established by the IACUC of Lanzhou University Second Hospital, formally known as the Animal Ethics Committee, and received approval. This study strictly adhered to the guidelines set forth by the “Animal Research: Reporting of In Vivo Experiments” (ARRIVE guidelines) for the reporting of standards and transparency in laboratory animal research (<https://arriveguidelines.org>).

Consent to participate

Informed consent was obtained from all individual participants included in the study.

Additional information

Supplementary Information The online version contains supplementary material available at <https://doi.org/10.1038/s41598-025-89235-2>.

Correspondence and requests for materials should be addressed to Y.X.

Reprints and permissions information is available at www.nature.com/reprints.

Publisher’s note Springer Nature remains neutral with regard to jurisdictional claims in published maps and institutional affiliations.

Open Access This article is licensed under a Creative Commons Attribution-NonCommercial-NoDerivatives 4.0 International License, which permits any non-commercial use, sharing, distribution and reproduction in any medium or format, as long as you give appropriate credit to the original author(s) and the source, provide a link to the Creative Commons licence, and indicate if you modified the licensed material. You do not have permission under this licence to share adapted material derived from this article or parts of it. The images or other third party material in this article are included in the article's Creative Commons licence, unless indicated otherwise in a credit line to the material. If material is not included in the article's Creative Commons licence and your intended use is not permitted by statutory regulation or exceeds the permitted use, you will need to obtain permission directly from the copyright holder. To view a copy of this licence, visit <http://creativecommons.org/licenses/by-nc-nd/4.0/>.

© The Author(s) 2025